Selective laser melting of a Fe-Si-Cr-B-C-based complex-shaped amorphous soft-magnetic electric motor rotor with record dimensions

(Article begins on next page)
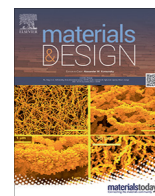
28 April 2024

Selective laser melting of a Fe-Si-Cr-B-C-based complex-shaped amorphous soft-magnetic electric motor rotor with record dimensions

Lena Thorsson [a], Mattias Unosson [a], María Teresa Pérez-Prado [b], Xueze Jin [b], Paola Tiberto [c], Gabriele Barrera [c], Bastian Adam [d], Nico Neuber [d], Amirhossein Ghavimi [d], Maximilian Frey [d], Ralf Busch [d], Isabella Gallino [d,*]

[a] Exmet AB, c/o Swerim, PO Box 7047, S-164 07 Kista, Sweden
[b] IMDEA Materials Institute, Calle Eric Kandel 2, 28906 Getafe, Madrid, Spain
[c] INRIM, strade delle Cacce 5, Torino, Italy
[d] Saarland University, Chair of Metallic Materials, Campus C6.3, 66123 Saarbrücken, Germany

HIGHLIGHTS

- Selective laser melting of an Fe-Si-Cr-B-C-based powder was used to additive manufacture a massive amorphous rotor.
- The rotor has record large dimensions for an amorphous alloy with diameter of 60 mm and height of 46 mm.
- The rotor has an internal complex shape to greatly facilitate the channeling of the magnetic flux.
- The rotor has extraordinarily high values of hardness of 877 HV.
- The measured soft magnetics are high magnetic susceptibility, small coercivity, and relatively high magnetic saturation.

GRAPHICAL ABSTRACT

Selective laser melting of a Fe-Si-Cr-B-C-based complex-shaped amorphous soft-magnetic electric motor rotor with record dimensions
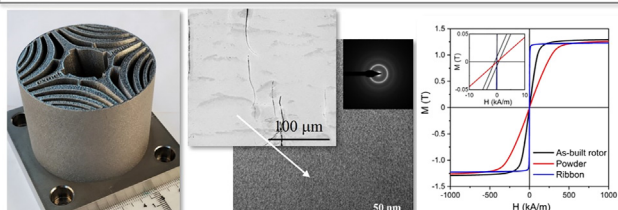
Rotor of 6 cm in diameter, complex 3D-geometry, 877 HV of hardness, and very soft magnetics: H_c=0.51 kA/m, M_s= 1.29 T, χ_{Hc} =9.7

ABSTRACT

A record large amorphous rotor bearing an intricate 3D-geometry is produced through additive manufacturing via selecting laser melting using a powder of a bulk metallic glass-forming composition of the Fe-Si-Cr-B-C system. Not only does this technique overcome the technical limitations characteristic of casting processes for amorphous alloys, but also the possibility to print complex 3D geometries is expected to greatly facilitate the channelling of the magnetic flux, when such component is used as a rotor in an electric machine. The rotor is characterized in comparison to the powder material as well as the as-spun ribbon using complementary techniques, including synchrotron x-ray diffraction, calorimetry, scanning and transmission electron microscopy as well as room temperature ferromagnetic and hardness testing. The rotor has extraordinarily high values of hardness (877 HV), high electrical resistivity (178.2 μΩ cm) and remarkable high magnetic susceptibility (9.17). This latter feature leads to a better magnetic response in the presence of an external magnetic field evidenced by a faster approach to saturation. The coercivity is relatively small (0.51 kA/m) and the magnetic saturation relatively high (1.29 T). In addition, a large anisotropic effect on the magnetization response in connection with partial crystallization in the melt pool areas is assessed experimentally.

* Corresponding author.
    E-mail address: i.gallino@mx.uni-saarland.de (I. Gallino).

1. Introduction

In every electric vehicle or device, the conversion of electric power into mechanical energy relies on soft-magnetic materials (SMM), since they are needed to enhance and/or channel the flux produced by the electric current [1–4]. An ideal SMM to be utilized as a passive component in an electric motor requires a certain, application-specific, combination of magnetic and mechanical properties. These properties typically include high magnetization saturation (M_s), small coercivity (H_c), high electrical resistivity, small magnetostriction, mechanical robustness or intrinsic ductility, high mechanical strength, and high hardness. Often compromises are made, e.g., high magnetic permeability or small power loss at the cost of a low M_s value, better magnetic properties at the cost of mechanical robustness, and/or sustainability at the cost of performance [3].

In addition, SMM components require complex 3-D geometries to channel the magnetic flux. Conventional processing routes, including casting and powder sintering, are mostly inadequate for this task. Still today, a common technology used for the manufacturing of electromagnetic systems is to assemble laminated magnetic circuits using plates, ribbon or wires, a task that is complex, time consuming and produces large amounts of scrap, i.e., waste of natural resources. In order to reduce time and resources, some more expensive manufacturing routes are currently implemented such as the production of composites made of iron powders, coated with an insulating polymeric binder that increases resistivity. These are obtained by consolidating the powders at high pressures. However, the mechanical strength is low and the magnetic flux paths are reduced which results in an overall poor soft-magnetic response [5]. Alternative methods for producing SMMs based on metal powders (crystalline and amorphous) typically involve direct AM methods such as the one applied in this study, which is Selective Laser Melting (SLM), or Laser Engineered Net Shaping (LENS) [6–11].

As early as in the late 1960 s it has been shown that amorphous metals or bulk metallic glasses (BMG) have excellent soft-magnetic properties, by far outperforming conventional crystalline soft magnetic alloys such as Si-steel or Fe-Si alloys (Fe-3 wt% Si) [3]. In comparison to these traditional materials, BMGs based on iron exhibit a unique combination of high resistivity ($\sim$3-times larger than that of Si-steel), near-zero coercivity, extraordinarily high hardness values ($\geq$800 HV) and strength (3 to 4 GPa of yield strength) as well as extraordinary high magnetic permeability ($\mu \approx 1.3$H/m), which is at least 3 orders of magnitude higher than Si-steel. The soft magnets made by BMG can operate with drastically reduced electrical power losses, which are related to the near-zero area under the M versus H hysteresis curve, and thus have the potential to serve in high-frequency applications.

The exceptional technological relevance of BMG as SMM is only limited by technical barriers related to the lack of industrial production routes to obtain amorphous metallic components of large dimensions and of complex geometries [3]. Currently, BMGs are mainly used in low-power applications where they compete with *permalloys* for the production of specialised small devices, mainly for sensing and switching. They also are used as transformers in some specific high-power applications.

Devices are assembled using thin metallic glass ribbons or wires of approximately 50 μm in thickness, obtained upon rapidly quenching by melt-spinning or by dropping a stream of molten alloy in a water/oil bath, respectively. In order to enhance the soft magnetic behavior, these ribbons are partially de-vitrified into nanocrystalline mixtures by post-heat treatment of the amorphous phase [2]. The microstructure of a partially nanocrystallised matrix cannot be precisely controlled and depends highly on heterogeneous nucleation mechanisms. In general, nanocrystallised ribbons show low saturation flux density compared to Si-steel, and high susceptibility to brittleness. A more important drawback is that the manufacturing of SMM components, involving cutting, stacking, or winding extremely thin and brittle laminations or wires, is known to be challenging and cost intensive.

Additive manufacturing (AM) methods such as SLM and LENS, utilizes a traveling laser beam to melt metal powders. By proper control of the laser process parameters, the exposed material will cool down immediately with a cooling rate of approximately 10^4 K/s after the laser spot has moved on. Hence, these AM methods are characterized by inherent quick solidification rates that facilitate the formation of amorphous microstructures in glass-forming compositions. AM is therefore considered to be a technology trigger in the field of metallic glasses because it can enable the production of complex components independent of the critical casting thickness for glass formation. In addition, the AM process parameters can also be adjusted to induce controlled regularly distributed nano-crystallisation on demand.

AM technique's enormous flexibility of the designed scheme endows these methods with great potential for the fabrication of parts with intricate geometries [12]. Recent studies have demonstrated, in particular, the suitability of SLM, also known and categorized as laser powder bed fusion (LPBF), for the production of BMG components of simple geometries, among others [13–23]. These works have investigated the relationship between processing parameters - such as the laser power and the hatch distance - and the fraction of crystallinity and defect structure for a few selected alloys. These basic investigations aimed to define processing parameters that allow the manufacturing of amorphous components of sizes that could exceed the critical casting thickness while simultaneously keeping crystallization, micro-cracking, and porosity below acceptable levels. This understanding is particularly critical for the production of robust passive components in electric motors, as it is well known that magnetic properties such as M_s or H_c in BMGs are highly dependent on the fraction of crystallites present and that defects can severely impair their structural capacity.

In this work, a step forward was taken by producing a massive SMM rotor bearing a complex 3-D geometry that cannot be obtained neither by casting nor by injection moulding. The rotor was successfully manufactured via SLM using a Fe-Si-Cr-B-C-based commercial amorphous powder. The elements of this systems are largely available and sustainable. For example, Co and rare elements like Nd are not included. The considered internal intricate design approach will allow us to move away from today's laminated structures, which is demanded to manage and minimise eddy-currents, toward monolithic ones. The rotor is characterized in this work using a wide range of complementary characterization techniques, including calorimetry, synchrotron x-ray diffraction, as well as scanning and transmission electron microscopy. The hardness, electrical resistivity and room temperature ferromagnetic properties of the rotor are measured and related to the microstructure developed during processing. This work opens new avenues for the design of complex metallic parts with outstanding magnetic functionality for sustainable mobility applications.

2. Material and methods

Fig. 1 illustrates a massive rotor that was additively manufactured in the present study via SLM. The rotor, a cylinder with a diameter of 60 mm and a height of 46 mm, exceeds the previously reported "record-large" Fe-based cylinder of Wang et al. [24]. The complex internal geometry of the rotor is a notable additional feature designed specifically to manage and minimize eddy currents.
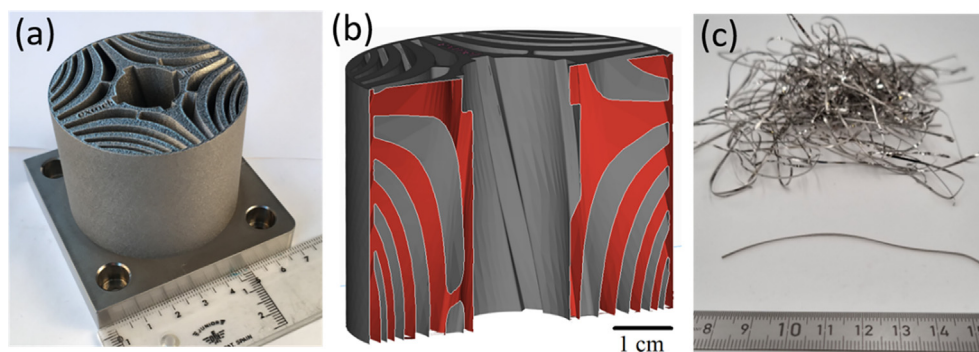
Fig. 1. AM-processed rotor versus as-spun ribbons produced for this study. Both with the composition of Fe$_{73}$Si$_{11}$Cr$_2$B$_{11}$C$_3$ at.%. (a) Photograph of the rotor still bonded to the build platform next to a centimeter ruler. The rotor has an outer diameter of 60 mm. (b) The internal design of the rotor on a vertical cross-sectional plane, parallel to the build direction. (c) Photograph of the amorphous melt-spun ribbons with an average thickness of 38 ± 2 μm.

The part was produced by SLM using a commercial AM-machine (EOS M290, 400 W Yb-fiber laser) and commercial magnetic powder of industrial grade quality with overall composition Fe$_{73}$Si$_{11}$-Cr$_2$B$_{11}$C$_3$ at. %, produced using the method described in Ref. [25]. The particle size distribution had a maximum size of 53 μm and a median particle diameter d$_{50}$ of 23.5 μm. The powder was stored in the as-received packaging condition at room temperature prior to characterization and printing. The processing window for the SLM was defined based on the systematic application of a wide range of heat inputs, HI, where HI = P / (v h d) in J/mm^3. The parameters P, v, h, and d, are the laser power, the laser scanning speed, the hatch spacing, and the layer thickness, respectively. While keeping d constant at 20 μm, P, v, and h were systematically optimized using a fractional factorial design of experiments ranging from 80 to 370 W, from 800 to 6000 mm/s and from 0.05 to 0.15 mm, respectively. The SLM processing was conducted in an Ar-atmosphere, with less than 0.1 % oxygen remaining in the building chamber.

As a reference, melt-spun ribbons with the same composition as the rotor were produced for this study. A pre-alloy ingot was prepared by arc-melting mixtures of Fe (99.97%), Si (99.9995%), Cr (99.98%), B (99.9%), and C (99.9%) on a water-cooled copper mould under a Ti-gettered Ar atmosphere. The pre-alloy was then inductively re-melted in a quartz tube furnished with a nozzle (0.8 mm diameter) under vacuum and subsequently injected onto a rotating copper wheel by applying high-purity Ar. The produced ribbons have a thickness of about 38 ± 2 μm (see Fig. 1c).

In-situ high-energy x-ray scattering experiments (HE-XRD) were carried out at the German electron synchrotron in Hamburg (DESY). The structure of the samples was investigated in transmission at the high intensity beamline facility P21.1 at PETRAIII. The powder material was placed onto a TESA film. In the case of the rotor material, we have analysed three specimens by HE-XRD. These were cut using electrical discharge machining from the base of the rotor, which is the part in contact with the building platform. Prior to the HE-XRD analysis, the specimens were manually polished and each specimen thickness was measured (~0.45 mm). Before the HE-XRD analyses, two of these samples were scanned in a differential scanning calorimeter (DSC) up to 837 K and 973 K, respectively, with 20 K/min and cooled with 180 K/min. The same three HE-XRD samples (1 as-built and 2 heat treated samples) were further analysed in terms of their magnetic response.

A wavelength of 0.124 Å (100 keV) with a beam size of 1 mm × 1 mm was used and the intensity was detected with a Perkin Elmer XRD1621 CsI bonded amorphous silicon detector (2048 × 2048 pixels). The two-dimensional x-ray diffraction patterns of the samples were integrated to obtain the intensity I(Q)

using the PyFAI analysis software. Further processing, such as background subtraction and correction for sample absorption, polarization, and multiple scattering was performed using the PDFGetX2 software [26]. The mean size $\hat{d}$ ordered crystalline domains is estimated according to the Scherrer equation: $\hat{d} = 2\pi K/\Delta Q$, where ΔQ is the full width at half maximum (FWHM) and K is the shape factor. We have fixed K = 0.9 in agreement with [27]. For the estimation of FWHM of the crystalline reflection observed in the as-built part the amorphous background of the fully amorphous powder was firstly subtracted and then the most prominent reflections are fitted to a Gaussian function following the procedures of [28].

Calorimetric measurements were performed using a Perkin Elmer Diamond DSC with a heating rate of 20 K/min in the range from 323 to 973 K under a constant high purity argon flux. The calorimeter was calibrated for the applied measuring conditions and for the applied pans (alternatively Al and Cu) for temperature and enthalpy of reaction using standards, i.e., In, Zn, and K$_2$SO$_4$.

The microstructure of the rotor was first characterized along a cross-section parallel to build direction (BD) by scanning electron microscopy (SEM) using a focused ion beam field emission gun scanning electron microscope (FIB-FEGSEM, FEI Helios NanoLab DualBeam 600i), utilizing an accelerating voltage of 30 kV, and a beam current of 2.7nA. The samples for SEM examination were prepared by standard metallographic techniques, including grinding with increasingly finer SiC papers. Second, the occurrence of crystallization was examined by transmission electron microscopy (TEM) using a FEI Talos F200x microscope operating at 200 kV. TEM lamellae were FIB-milled at selected regions using a trenching-and-lift-out method following the steps summarized in [29]. TEM characterization was carried out both in bright field mode, with a parallel beam, as well as in scanning transmission (STEM) mode, with a high angle annular dark field (HAADF) detector. Energy dispersive x-ray spectroscopy (EDS) was used in order to map the local distribution of alloying elements.

The Vickers hardness of the rotor was evaluated in the as-built condition along a plane perpendicular to the build direction and, in particular, along the two perpendicular diameters of the rotor. A total of 88 measurements were performed using a Shimadzu microhardness tester with a load of 1000 g and a dwelling time of 15 s. Before microhardness testing, the top surface of the rotor was ground and mechanically polished in order to avoid the effect of surface roughness.

Room temperature hysteresis loops were measured by a high-sensitivity vibrating sample magnetometer (LakeShore mod. 7400–VSM, with instrument magnetisation sensitivity in 10^{-7} emu), by applying a magnetic field in the range ± 1000 kA/m. The magnetic measurements were performed on the as-received

metal powder, on the three HE-XRD plates (1 as-built and 2 heat treated samples by DSC) obtained by cutting the rotor, and on the amorphous as-spun ribbon. For the rotor samples, the magnetic measurements were performed by applying the magnetic field (H) both perpendicular to the SLM build direction (in-plane) and parallel to build direction (out-of-plane). The magnetization value was normalized to the sample volume, calculated by means of sample weight and material density measurements.

Room temperature resistivity was evaluated via measuring the voltage drop and calculating the contact resistance in accordance to the International Standard IEC 660512–2–1 procedures. Five cylindrical samples with diameter 10 mm and length 22 mm were AM-processed using the same SLM-machine, same powder alloy, and same laser process parameters as the rotor part. The voltage drop was measured by applying a 1 A Direct Current (DC) and measuring over a central section of the sample. The measurements were performed at room temperature using a digital multimeter (Keithley 2700), and the current source was a ripple-free Kenwood P20. Three pairs of measuring probes, placed 10 mm apart and evenly distributed over the circumference, were used simultaneously to achieve a reliable result. The average voltage drop was calculated for the five samples using both forward and reverse current and values for all three probe pairs. The resistivity was estimated under the assumption that the current was evenly distributed over the cross section in the part of the sample where the measurement was performed.

The density of the AM-processed material was evaluated using the Archimedes method using a Sartorius MC 210P scale equipped with a density kit, also supplied by Sartorius. For this measurement, two large solid cubes were produced by using the same SLM-machine, the same SLM parameter set and the same powder as used to produce the rotor. Each measurement was repeated three times. The average density for these six measurements was calculated to be 7.035 ± 0.003 g/cm^3, which is consistent with the density value of the powder provided by the supplier.

3. Results

Fig. 2 shows the normalized HE-XRD intensity data of this study. In the x-ray intensity pattern of the rotor in as-built condition, some broad Bragg-peaks are present above the amorphous background. The strongest reflections are indicated in Fig. 2a with symbols and correspond to those of the Fe-rich compound Fe$_3$Si, followed by Fe$_2$B and the metastable Fe$_{23}$B$_6$. For the analyses the PDF 00–045-1207 (for Fe$_3$Si), PDF 04–003-4132 (for Fe$_2$B) and PDF 01–074-3231 (for Fe$_{23}$B$_6$) of Ref. [30], were used. This indicates that the rotor material consists mainly of an amorphous matrix with embedded nanoscale crystalline compounds rich in Fe, whose reflections grow in intensity when the amorphous matrix starts to crystallize at high temperature. The powder and the as-spun ribbon (see Fig. 2b) are both fully synchrotron-amorphous because Bragg-peaks connected to crystalline reflections are absent.

Fig. 3 shows the subtracted differential scanning calorimetric (DSC) heat flow scans for the rotor, the powder and the ribbon performed with a heating rate of 20 K/min. The rotor material (black curve) and the ribbon (blue curve) are in the as-printed and as-spun conditions, respectively. The powder material (red curve) is in the as-received condition.

The heat flow scans shown in the inset of Fig. 3 were performed in Al-pans up to 873 K. Up to this temperature, only the main first crystallization event (X1) is detected for the applied heating rate, however the use of Al-pans resulting in resolving the Curie temperature and the glass transition, which is hardly detected with Cu-pans. These characteristic temperatures are listed in Table 1. The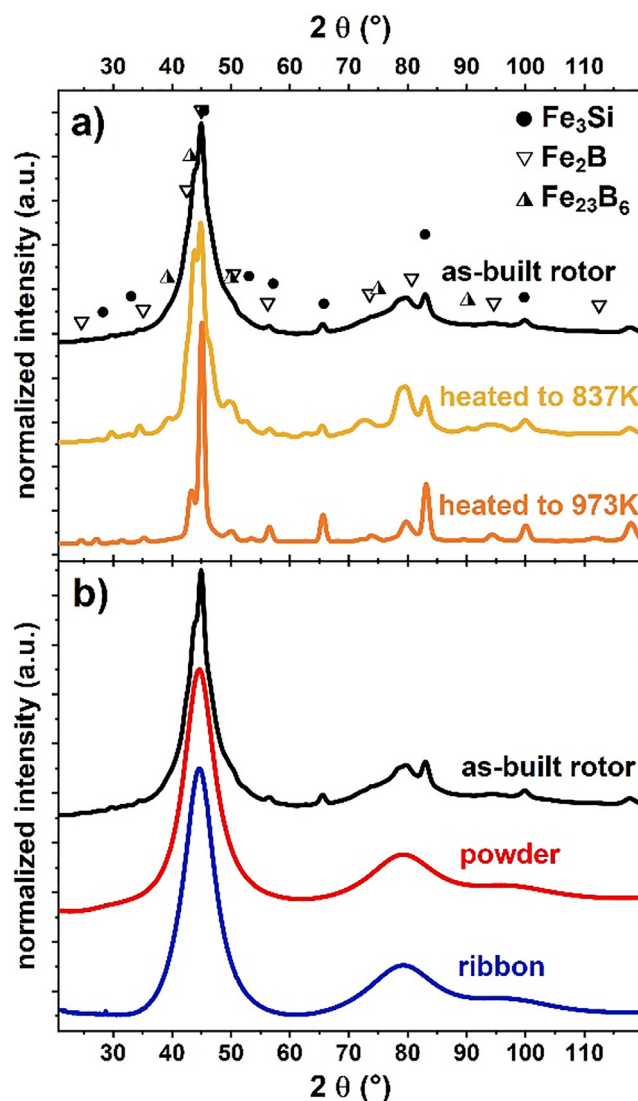 DSC in Cu-pans are performed up to 973 K and show that additional small crystallization events follow the main crystallization event and this also contribute to the total enthalpy released during crystallization (ΔH_X). It should be noted that the 70% amorphicity for the as-built rotor is assigned in Table 1 based on a comparison between the ΔH_x values of the rotor and the ribbon. The 100% amorphicity for the powder and the ribbon is assigned based on the HE-XRD results of Fig. 2b.

The heat released during crystallization of the amorphous matrix, ΔH_X, is obtained by integrating the total exothermic event. The rotor material releases less heat during crystallisation than the fully amorphous ribbon because it is already partially crystalline after the AM processing in accordance with the structural results of Fig. 2. A comparison between the ΔH_X values of the rotor (-5.3 kJ/mol of atoms) and the ribbon (-7.5 kJ/mol of atoms) gives a percentage of the amorphous phase of approximately 70% for the rotor material.

Fig. 2. Normalized high-energy x-ray intensity data. (a) The rotor of composition Fe$_{73}$Si$_{11}$Cr$_2$B$_{11}$C$_3$ at.% in as-built conditions and after heat treatment as indicated. The rotor material shows some small and broad Bragg-peaks beside the amorphous background, which are assigned to Fe$_3$Si, Fe$_2$B and Fe$_{23}$B$_6$ based on Ref. [31]. After heating to 837 K the amorphous background is still visible and only the reflections associated with Fe-B-based compounds have increased in intensity. After heating up to 973 K the rotor material appears completely crystallized and the Fe$_3$Si reflections have grown in intensity. (b) As-received powder and as-spun ribbon showing only the amorphous background, in comparison to the rotor in as-built conditions.
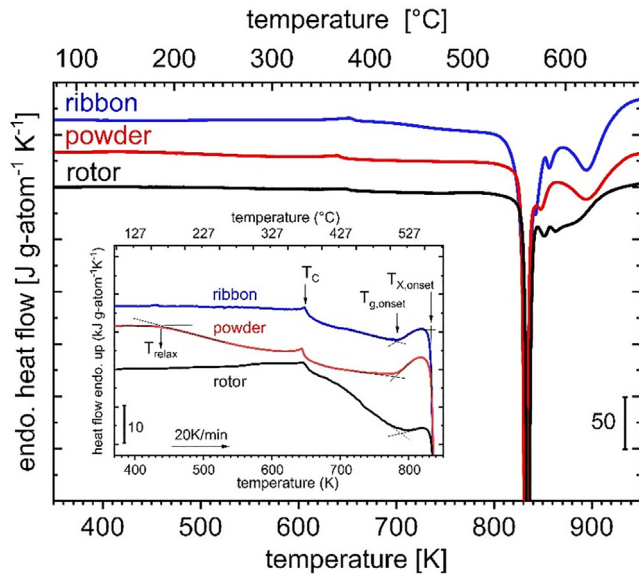
Fig. 3. Molar heat flow DSC up-scans of the rotor material (black curve), powder (red curve) and ribbon material (blue curve) of composition $Fe_{73}Si_{11}Cr_2B_{11}C_3$ at.% using a heating rate of 20 K/min. The DSC scans are performed in Cu pans up to 973 K and show one main peak followed by multiple small crystallization events. (Inset) Magnified heat flow signals in the low-temperature regime performed in Al-pans to better identify the characteristic temperatures for the onset of enthalpy relaxation (T_{relax}), the Curie temperature (T_C), the onset of the glass transition ($T_{g,onset}$), and the onset of crystallization ($T_{X,onset}$), respectively, based on the tangent construction method as indicated.

Fig. 4 shows an SEM micrograph that is representative of the microstructure of the rotor along a plane parallel to the build direction (BD). This image illustrates a homogeneous distribution of microcracks that are parallel to the BD. The average microcrack length is 101.5 ± 5.9 μm, hence approximately five layer thicknesses, and the average distance between microcracks, measured along a direction perpendicular to the BD, is 88.2 ± 8.8 μm. In addition, Fig. 4 shows the presence of some elongated regions (5 to 10 μm thick), with darker grey contrast and perpendicular to the BD, that are dispersed within a matrix that appears with light grey color in the micrographs. The average distance between such regions, measured along a direction parallel to BD is 29.9 ± 2.1 μm.

A detailed analytical TEM analysis was carried out (Figs. 5-7) in order to investigate the origin of the stripes with grey contrast apparent in the SEM micrographs. Fig. 5 illustrates, first, the microstructure of the matrix, which appears with lighter grey contrast in Fig. 4. It can be clearly seen that these areas are fully amorphous, which is indicated by the presence of diffuse rings in the selected area electron diffraction pattern (SAED) of Fig. 5.

Fig. 6a shows the microstructure of a FIB-milled lamella that was extracted for one of the thickest grey stripes, as indicated in the corresponding inset. It contains several crystalline zones with different nanocrystallite morphology and composition (Fig. 6.b-d), which result from the temperature gradient in the heat-
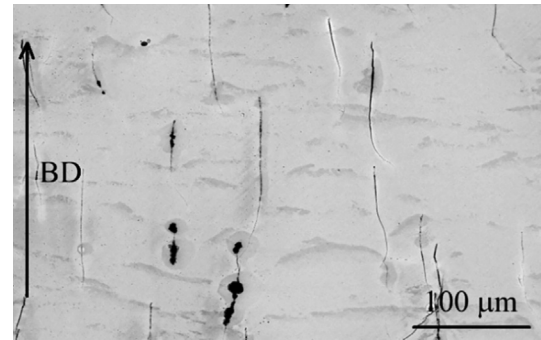

Fig. 4. SEM micrograph. Illustrating the microstructure of the $Fe_{73}Si_{11}Cr_2B_{11}C_3$ at.% rotor along a plane parallel to the build direction (BD). Small microcracks and pores are aligned parallel to each other and to BD, whereas the grey stripes, associated with nano-crystallized regions within the heat-affected zones are perpendicular to BD.
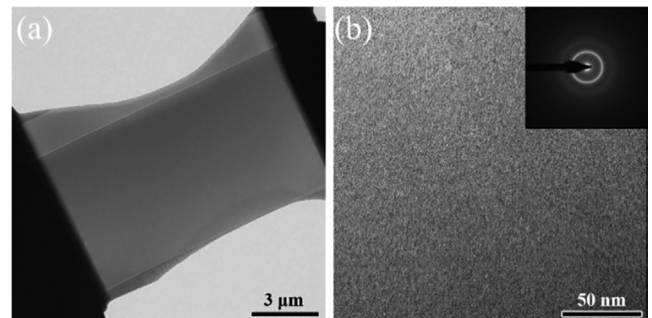

Fig. 5. TEM micrographs corresponding to the amorphous matrix. (a) Lamella overview extracted in a region that in SEM showed a brighter contrast. (b) A local closer view, representative of the entire lamella. The inserted figure shows the corresponding selected area diffraction (SAED) pattern typical of an amorphous structure.

affected zone that is inherent to the layered SLM process. Based on these images, the size of the nanocrystallites ranges approximately from 20 to 200 nm, with most having rather small sizes. Only a few nanocrystallites were able to grow to the maximum observed size in regions with a large local temperature increase. The fact that they were not detected by HR-XRD in Fig. 2, denotes that their fraction is very small. These were found towards the top of the analysed dark grey areas, i.e. in the vicinity of the next freshly built amorphous layer (labeled as 'layer n + 1' in Fig. 6a). The presence of the mentioned nano-structures gives rise to distinct spots in the SAED pattern reflecting individual crystal planes in the nanocrystalline structure. Nanocrystallites appear in the bright field micrographs of Fig. 6 with brighter and darker grey contrast, reflecting the presence of different compositions, which are examined in more detail below in Fig. 7. It is worth noting that the fraction of crystallites with brighter grey contrast increases in the areas located towards the top of the crystallized regions, i.e., in

Table 1
DSC results probed with a heating rate of 20 K/min. Characteristic temperatures (errors on the order of ± 0.5 K) and enthalpy of crystallization ΔH_X (errors on the order of ± 0.4 kJ/mol of atoms) T_{relax} is the onset temperature of enthalpy relaxation. T_C is the Curie temperature. $T_{g,onset}$ and $T_{X,onset}$ are the onset temperature of the glass transition and crystallisation, respectively. T_{X1} and $T_{X,end}$ are the peak temperature of the main crystallization event and the end temperature of the overall crystallization event, respectively.

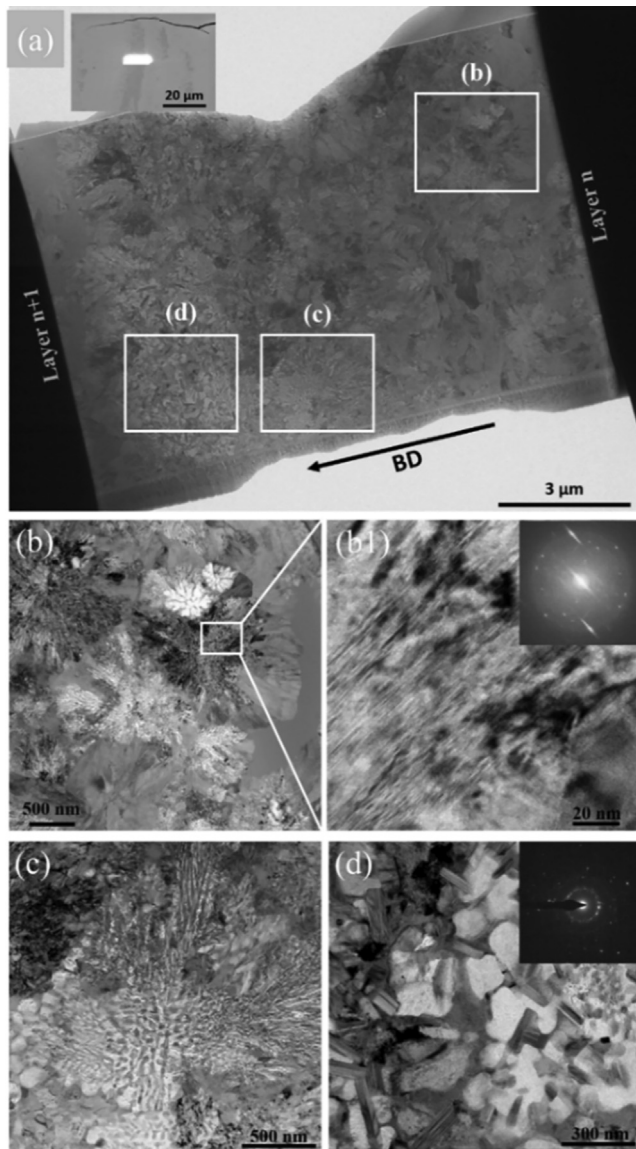|	T_{relax}	T_C	$T_{g,onset}$	$T_{X,onset}$	T_{X1}	$T_{X,end}$	ΔH_X	amorphicity
units	K	K	K	K	K	K	kJ/mol	%
Rotor	437	648.2	789.2	833.3	845.2	920.2	−5.3	70
Powder	437	644.2	781.8	833.2	841.2	930.0	−7.2	100
Ribbon	N/A	648.2	784.7	833.3	843.4	933.7	−7.5	100

Fig. 6. Bright field TEM micrographs corresponding to the nano-crystallized region. (a) Overview of a lamella extracted from a region of one of the grey stripes that in SEM showed a darker contrast. The inserted SEM micrograph on the top left shows the exact location where the lamella was FIB milled (bright spot). BD is the build direction. The positions of the images in panels b-d are framed. (b) Crystallized region towards the bottom of the heat-affected zone showing at higher magnification in (b1) a very fine non-equilibrium nanocrystalline microstructure. (c) Intermediate coarse dendritic nanocrystalline microstructure. (d) Coarsest nanocrystalline microstructure at the top of the heat-affected zone. The inserted images in (b1) and (d) are the corresponding SAED patterns, which show nanocrystalline diffraction spots.

the regions that were subjected to a higher temperature increase during the building of subsequent layers.

Fig. 7 illustrates, qualitatively, the composition of the coarser nanocrystallites found in Fig. 6(d) by means of TEM EDS elemental maps. In particular, this figure shows that the bright coarse grains are rich in Fe and Si and they are depleted of C and B, whereas the darker grey grains are rich in Fe, B, and Cr. The latter grains show extensive twinning and they seem to act as nucleation sites for the formation of Fe_3Si, in agreement with the recent AM work of Ł. Zrodowski et al. [16] with a similar Fe-based composition however with simple geometry.

Room-temperature hysteresis loops, measured in the powder (red curve), as-built rotor (black curve), and as-spun ribbon (blue
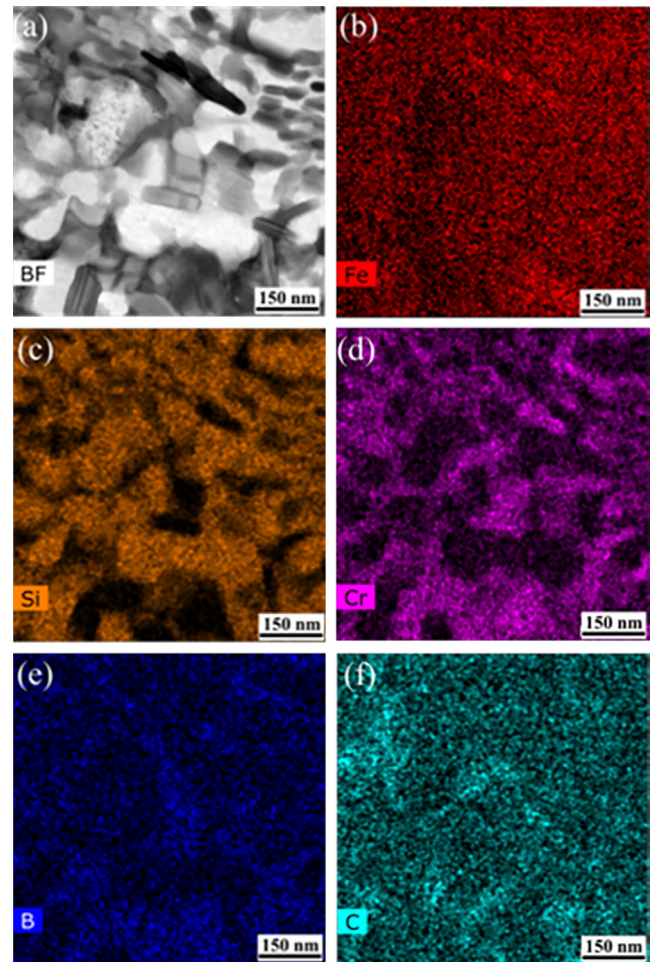

Fig. 7. EDS measurement of elemental maps within the nanocrystalline region. (a) Bright field micrograph illustrating the region where elemental mapping was carried out; (b) Distribution of Fe; (c) Distribution of Si; (d) Distribution of Cr; (e) Distribution of B; (f) Distribution of C.

curve) are shown in Fig. 8, respectively. A comparison between the magnetic response obtained by applying the magnetic field along the in-plane direction (H perpendicular to the build direction) and out-of-plane direction (H parallel to the build direction) is shown in Fig. 9. Table 2 summarizes the main features of magnetic hysteresis for all of the studied samples, i.e., saturation magnetization (M_s), magnetic remanence (M_r), M_R/M_S parameter, coercive field (H_c), and initial magnetic susceptibility (χ_{Hc}) evaluated around H_c. These values are discussed in section 4.4, however from a quick comparison between the AM-process rotor and the starting powder it appears that the magnetic response in presence of a magnetizing external field is higher for the rotor as indicated by the higher value of χ_{Hc} and of M_s, which means that the rotor has improved soft-magnetic response with respect to the starting powder, even though the rotor is not 100 % amorphous. An optimized additive manufacturing process that may imprint a higher percentage of amorphicity will result in improved soft magnetic properties, i.e. a lower coercivity value and a steeper approach to saturation, as the ribbon response indicates in Fig. 8. The evolution of the magnetic properties following heating in the DSC up to the indicated temperatures is shown in Fig. 10, where a comparison between the room-temperature in-plane hysteresis loops of the three samples is reported. The heating process leads to a similar increase in the coercivity for the two temperatures that were analysed. Conversely, the M_s values decrease slightly with increasing temperature.
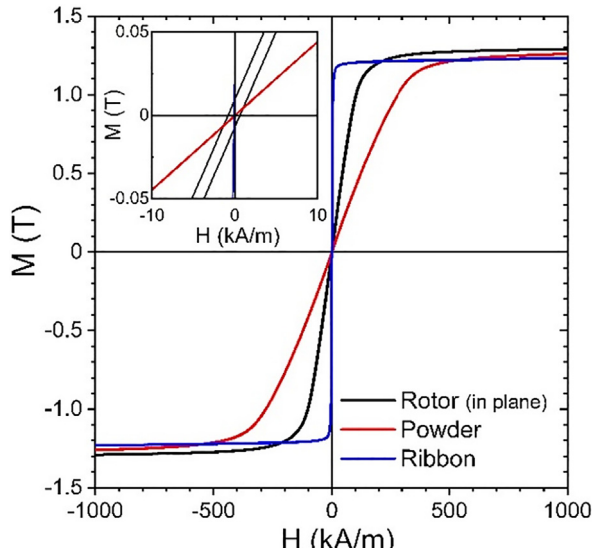
Fig. 8. **Room-temperature hysteresis loops** of the AM-built rotor material (black curve) in comparison with the powder material (red curve) and the as-spun ribbon for the alloy composition $Fe_{73}Si_{11}Cr_2B_{11}C_3$ at.%. The inset plot is a magnification for small H values.

Fig. 10. **Room-temperature hysteresis loops** along the in-plane direction for the rotor in as-built condition (black curve) and after crystallization via heat treatment up to 837 K (green curve) and 973 K (red curve). The inset plot is an enlarged view of the small H region.

The Vickers hardness of the rotor was evaluated in the as-built condition along a plane perpendicular to the BD after grinding and polishing and, in particular, along the two perpendicular diameters of the rotor, as shown in Fig. 11. The results were found to be consistent along these two selected diameters. An average value of HV of 876.9 ± 83.5 was calculated from a total of 88 measurements. The scatters in the data may be attributed to the presence of described amorphous/nanocrystalline layered structure, as well as to the presence of scattered sub-surface defects.

4. Discussion

4.1. Multiscale design and properties

This work demonstrates that a 'record-large' amorphous rotor with a dimension beyond the critical casting thickness of the glass forming system and with complex geometrical and microstructural features of various scales was manufactured via laser-based additive manufacturing – a result that is impossible to achieve by other manufacturing processes.

On the *macroscale level*, i.e. in from 0.1 to 2 mm range, the intricate internal design of our additive manufactured soft magnetic component should enable us to transition from laminated to monolithic structures in electric power conversion applications. The intricate 3D design shown in Fig. 1b can greatly reduce eddy-current losses when the component is subjected to an alternating magnetic field, in agreement with the recent work of Plotkowski et al. [32] on additive manufacturing of crystalline Si-
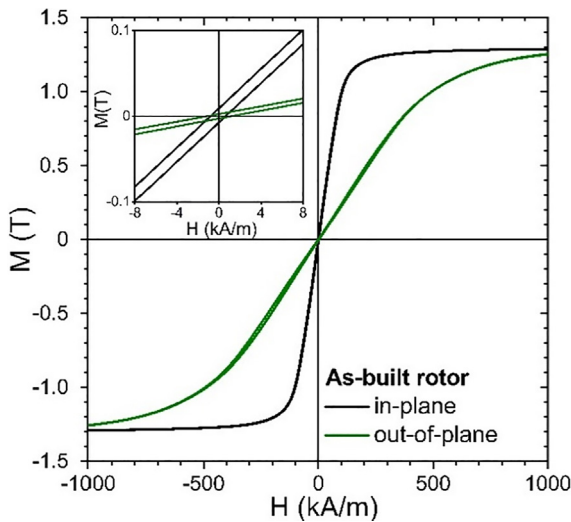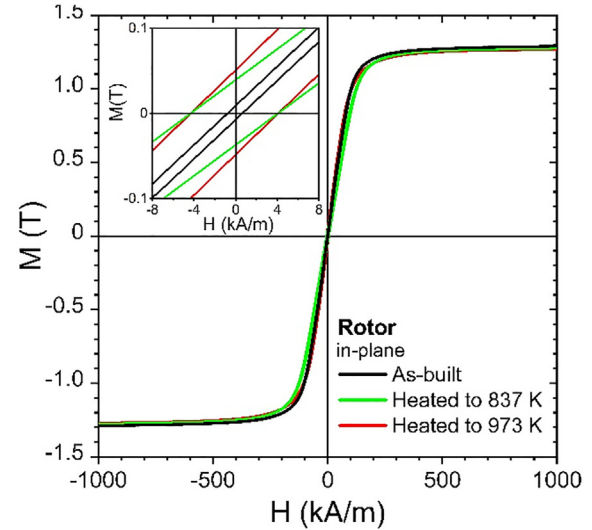

Fig. 9. **Room-temperature hysteresis loops** of the AM-built rotor material along the in-plane (black curve) and out-of-plane (green curve) directions. The inset plot is an enlarged view of the small H region.

The average resistivity of additive manufactured material was measured to be 178.2 ± 2.1 $\mu\Omega$ cm. This value agrees with as-cast or as-spun Fe-based glasses [31] and it is at least 3 times greater than the resistivity of Si-steel [1].

Table 2
Characteristic magnetic properties of the powder and the as-built BMG alloy. Magnetic saturation (M_s), magnetization remanence (M_R), coercivity (H_c), magnetic susceptibility (χ_{HC}), measured from the data shown in Fig. 8.

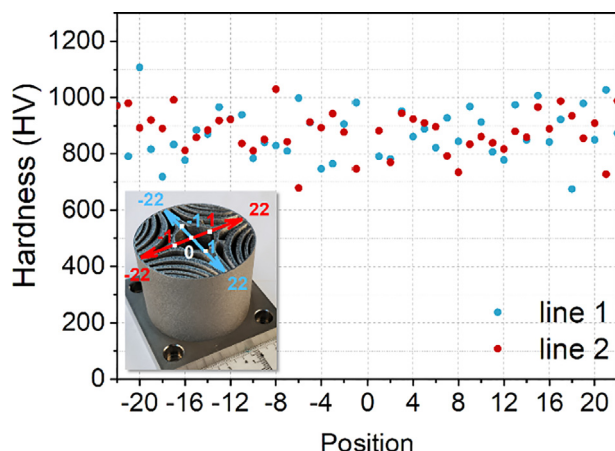|	M_S	M_R	M_R/M_S	H_C	χ_{HC}
Units	T	T	dimensionless	A/m	dimensionless
Powder	1.27	3.50×10^{-5}	2.76×10^{-5}	61	3.51
Rotor: as-built(in-plane direction)	1.29	8.25×10^{-3}	6.40×10^{-3}	510	9.17
Rotor: as-built(out-of-plane direction)	1.29	2.60×10^{-3}	2.02×10^{-3}	1000	1.76
Rotor: heated to 837 K(in-plane direction)	1.27	3.80×10^{-2}	3.00×10^{-2}	4200	7.20
Rotor: heated to 973 K(in-plane direction)	1.27	5.00×10^{-2}	3.94×10^{-2}	4200	9.38
Ribbon	1.22	3.30×10^{-3}	2.75×10^{-3}	< 50	252

Fig. 11. Room-temperature hardness measurements along the indicated lines.

steel. In comparison with Si-steel, however, an amorphous rotor can operate with extremely low electric power losses [3] because of a few improved material electromagnetic properties typical for amorphous components, i.e., high resistivity of 178.2 μΩ cm, very high magnetic permeability of 1.3H/m, relative permeability at 1 kHz in the range of 1×10^4 to 5×10^4, remaining larger than 10^3 at 100 kHz and low coercivity [31]. This means that our new rotor design has great potential to decrease power losses in electric power conversion applications by an unprecedented value that is expected to be as high as 80% [3] and thus can disrupt traditional soft-magnetic materials.

On the *mesoscale level*, i.e., in the range between 1 and 100 μm, fully amorphous layers are alternated with thin crystalline layers (thickness < 10 μm) containing nanocrystalline compounds rich in iron, lying parallel to each other and perpendicular to the build direction (see Fig. 4). The layer by layer building of the SLM process leads to the development of an amorphous metal matrix and alternating Fe-rich nanocrystalline layers, which is not possible to achieve via casting. In the next section, this concept is developed further.

On the *nano-scale* (<1 μm) down to the atomic scale, the results show that about 70% of the rotor material has an amorphous structure (see Table 1). The crystalline regions are, furthermore, confined to thin parallel layers within the amorphous matrix and therefore the fabricated composite bears the typical superior soft-magnetic properties of iron-rich amorphous alloy compositions in combination with extraordinary mechanical hardness of 877 HV (this study) and strength (3 to 4 GPa of yield strength according to [31]) and high electrical resistivity of 178.2 μΩ cm (this study).

In Fig. 2 the strongest HE-XRD reflections found in the as-built rotor material correspond to those of the Fe-rich compound Fe_3Si, followed by Fe_2B and the metastable $Fe_{23}B_6$. The mean size $\hat{d}$ of each of these ordered crystalline domains is estimated according to the Scherrer equation (see methods) as 9.5 ± 0.4 nm, 7.9 ± 0.2 nm, and 8.9 ± 0.4 nm, for Fe_3Si, Fe_2B, and $Fe_{23}B_6$, respectively. The nanometre size (<10 nm) for the mean size of the majority of the ordered domains indicates that they have formed when the amorphous phase is re-heated during subsequent passes and not during cooling from above the melting point, which would have formed larger size crystallites in the order of 10 μm or larger, in agreement with Schroers et al. [33].

4.2. SLM processing-induced crystallization

As discussed above, the as-built part is amorphous with embedded Fe-rich nanocrystals. The nanocrystals are not distributed homogeneously but their appearance is exclusively confined to specific zones subjected to an intrinsic heat treatment during the melting of subsequent layers. The crystallized regions contain many different crystalline zones, as a result of an induced temperature gradient. The (n + 1) laser pass is able to re-melt the very top part of the n layer, while the high cooling rate of the SLM processing ($\sim 10^4$ K/s) is able to freeze the liquid structure again. It is in the region directly underneath that it is not re-melted, but acts as a heat sink, where crystallization of the amorphous phase takes place far below the melting point.

If we consider the x-ray patterns in Fig. 2 after post-processing heat-treatment (by means of calorimetry), it is evident that the amorphous matrix crystallizes in two steps. After heat treatment up to only 837 K (between $T_{X,onset}$ and T_{X1}), the reflections that belong to Fe_3Si have increased only slightly with respect to their counterparts in the as-built part, whereas those of Fe_2B and $Fe_{23}B_6$ show a relatively large intensity increase. After the heat treatment up to 973 K, i.e., after full completion of the crystallization process, it can be seen that the amorphous halo has disappeared and that the Fe_3Si x-ray reflections have grown disproportionately in comparison with the reflections of the Fe_2B and $Fe_{23}B_6$ compounds.

This suggests that the solid-state nucleation and growth of Fe_3Si is activated at elevated temperatures. According to the TEM analyses of Fig. 6d and 7, Fe_3Si formed and grew preferentially in the hottest part of the heat affected zone, leading to sub-micron sized crystals. More internally towards the bottom of the thermally altered zone, the material was subjected to a lower temperature increase and there in fact the phases Fe_2B and $Fe_{23}B_6$ preferentially nucleate. In this case, Si is rejected into the matrix *via* atomic partitioning [34–35] and locally thermodynamically destabilize the surrounding amorphous phase and favor the nucleation of very fine Fe_3Si nanocrystals. Reflections that could be assigned one-to-one to C- or Cr-bearing compounds appear to be absent from all HE-XRD patterns. These two elements seem to act as solute elements in the binary compounds, which is typical for crystallized metallic glasses [36]. On the basis of the TEM EDS analyses, it is evident that Cr is found in grains where B is mostly enriched (Fe-B grains) and Si depleted (see Fig. 7c-d-e in comparison). C appears to be more homogeneously distributed (Fig. 7f).

4.3. Calorimetric study

According to the heat flow signals of Fig. 3, an exothermic broad signal starts at around 437 K, which is marked with T_{relax}. This is very evident for the powder material and less for the ribbons. This is connected to an enthalpy relaxation process during physical aging of the quench-in glassy matrix [37–39]. The area underneath the relaxation signal is a measure of the enthalpy released during relaxation. It appears that the powder is relaxing more than the other two specimens, which agrees with the ultrafast applied cooling rate during gas atomization. The slight decrease of T_C by $\approx$ 4 K observed in the powder material could be ascribed to a weakening of the magnetic order due to the much higher surface/volume ratio in the powder sample with respect to the massive rotor and ribbon samples. The onset of the glass transition and crystallization are basically the same for all three materials, confirming that the nature of the amorphous matrix is the same.

The overall enthalpy of crystallization ΔH_X is obtained by integrating the area under the overall crystallization signal. The value of ΔH_X for the powder and the ribbon is − 7.2 and − 7.5 kJ g-atom^{-1} (where 1 g-atom^{-1} = 1 mol of atoms), which agrees with other Fe-based metallic glass systems [40]. The ΔH_X for the rotor material is − 5.3 kJ g-atom^{-1}, which is approximately 70% of that of the ribbon, indicating that the rotor is partially amorphous and partially crystalline, with about 30% of crystallinity. Based of the x-

ray investigations shown in Fig. 2, the DSC crystallization peaks are assigned as follow. The main exothermic event (X1) represents the nucleation of the B-containing intermetallic phases, whereas the following steps seem to be connected mainly to the nucleation and growth of Fe_3Si.

4.4. Soft-magnetic properties

The magnetization process in this study was measured in quasi-static conditions. The fully amorphous iron-based ribbon (blue curve in Fig. 8) behaves as an extremely soft magnetic alloy with a very high initial magnetic susceptibility together with a faint coercivity value. The latter is not detectable due to the high-field scale provided by the applied experimental technique that is not sensitive at a very low field (A/m).

Fig. 8 shows that all samples reach almost the same magnetization saturation values, see Table 2. The as-built rotor displays a hysteresis (black line) with a magnetization saturation value (M_s) slightly higher with respect to the powder material with which the rotor was built as well as with respect to the as-spun ribbon having the same composition of the powder. In general, fully amorphous iron-based alloys are characterized by higher M_s [41], with the exception of the so-called nanocrystalline alloys such as FINE-MET [42]. Moreover, the M_S value of the rotor (≈ 1.29 T) is slightly higher than that typical of as-cast bulk metallic glasses having almost the same Fe content [43]. This feature can be attributed to the presence of iron-rich nanocrystalline grains as revealed by XRD patterns (mostly Fe_3Si, Fe_2B). The same trend is observed for the magnetization remanence (M_R) in the as-built rotor and ribbon whose low values indicate a substantial demagnetized state at H = 0 Oe, which must be induced by an almost complete random orientation of the magnetic moment in the magnetic domains. This effect of randomness is enhanced when the sample is in the form of a powder, leading to a further reduction of the M_R value. These evidences are also confirmed by a similar relationship between the M_R/M_S values in Table 2.

Conversely, the magnetic susceptibility (χ_{Hc}), considered one of the most important parameters in electrical machines, markedly changes in the three studied samples. The amorphous ribbon displays the highest χ_{Hc} value, whereas the powder and the as-built rotor clearly show a different approach to saturation as confirmed by the value of magnetic susceptibility (χ_{HC}) taken at the coercive field. In particular, the χ_{HC} value turns out to be nearly double in the rotor than in the powder, thus resulting in a slower approach to saturation in the latter (Fig. 8). This leads to a lower value of the applied magnetic field needed to reach magnetisation saturation for the rotor. It is important to note that the as-built rotor displays a χ_{Hc} value higher than that of the completely amorphous powder from which it was built (i.e. same overall composition). This difference in the magnetization process can be explained in terms of microstructural differences. In particular, the domain structure of individual grains of the fully amorphous powders is multidomain, therefore inducing an independent magnetization process in all grains contained in the measured volume. On the other hand, the as-built rotor is characterized by a homogenous alternating of fully amorphous regions and layers containing iron-based nanocrystalline grains. This leads to a higher value of χ_{Hc} with respect to the powder. Microstructure differences also affect the coercivity value. In fact, H_c turns out to be negligible in the powder (≈ 61 A/m), in agreement with Ref. [16], where, reportedly, an amorphous powder material with similar composition as the one of this study has exhibited an H_c value of 99 A/m. The rotor is characterized by a value of H_c of approximately 510 A/m (see inset of Fig. 8 and Table 2), which is still in the range of very soft magnetics alloys, i.e. 100–1000 A/m [1]. This increase may be ascribed to the magnetic domain pinning effect by the layer containing the nanocrystalline grains.

As a matter of fact, the magnetization process in ferromagnetic systems is controlled by domain wall movements. Grain boundaries are expected to pin the magnetic domain walls, inducing a slightly higher coercivity value, and therefore a higher field is needed to displace the walls. In fully amorphous alloys, this movement is less hindered and, in the ideal case, it should be completely free leading to a zero coercive field [44]. The characteristic magnetic properties of the rotor, reported in Table 2, which are measured under static conditions, have values that correspond to those that are usually characteristic of soft magnets used in electrical machines [45]. Such a promising performance has to be sustained by a comprehensive study of power losses as a function of frequency.

In addition, for the as-built rotor, an anisotropic behavior is found in room-temperature hysteresis loops measured in the two geometrical directions (see Fig. 9). Such evidence is ascribed to the effect of demagnetizing field intensity related to the sample shape and the high aspect ratio. This determines M_R and M_R/M_S values that are higher in the in-plane direction than in the out-of-plane direction.

Finally, in Fig. 10, the hysteresis loops of the as-built rotor and the two plates submitted to the heating process appear to be substantially the same with similar values of χ_{Hc} and M_s. In the inset, the low field magnification is shown and put in evidence an increase of magnetic coercivity and remanence magnetization of the two heated plates. Again, this increase may be ascribed to a further precipitation of boride-phases that mostly occurs at 873 K.

5. Conclusions

In this work, a soft magnetic component (rotor) is successfully manufactured *via* SLM by additive manufacturing using a commercial powder of the metallic glass forming Fe-Si-Cr-B-C system. This rotor bears record large dimensions for an amorphous alloy and a complex 3D-geometry on the macroscopic level. Both the structure and the microstructure of the built part are thoroughly characterized using a wide range of laboratory and synchrotron-based techniques and compared to an as-spun ribbon having the same composition.

The synchrotron HE-XRD investigations probed a very large volume of the material on the atomic level and identified that the mean size of the majority of the ordered domains in the amorphous matrix are less than 10 nm, which indicates that they have formed when the amorphous phase is re-heated during the layer by layer SLM process and not during cooling from above the melting point. On the other hand, SEM and TEM analyses probed very localized areas of the as-built part and proved that the AM-built material is made of a completely amorphous matrix that alternates with thin (<10 μm) nanocrystalline layers rich in Fe. The crystallisation is confined exclusively into these layers which are affected by heat during the SLM process. Therefore, the crystalline layers are all parallel to each other and perpendicular to the build direction. The continuous refinement of the microstructure from the top to the bottom of the heat affected zone was observed which is induced by a strong temperature gradient. This microstructure refinement agrees with [27], where the crystallization of a BMG system at a higher temperature, close to the nose for crystallization in a time–temperature-transformation (TTT) diagram, resulted in coarser equilibrium structures than the crystallization at temperatures much lower than the nose. DSC analyses showed that the percentage of crystallinity is approximately 30%.

The AM-built rotor exhibits exceptionally large and complex dimensions, extraordinary high hardness, high electrical resistivity

and very soft magnetics. The coercivity of the as-built rotor is 510 A/m, which is still higher than a fully amorphous ribbon material of same composition. This is expected to be decreased by a simultaneous refinement of the SLM parameters as well as the alloy composition specifically for the SLM process. In the condition reported here, the additional crystallization-induced magnetic anisotropy has to be considered as an additional design parameter that must be considered in the design of SMM components.

The major outcome of this study is that the AM process appears to increase the magnetic response in the presence of a magnetizing external field with respect to the starting powder as indicated by the higher value of χ_{Hc} and the M_s leading to a steeper M−H magnetization curve. Thus, such a feature induces an optimized, easier approach to saturation in the presence of a magnetic field (i.e. lower H value needed to reach M_s) and is a key point for electrical motors. This definitely compensates for the slight increase of H_c which is observed and consequently may limit the effect of the overall magnetic losses, another crucial parameter for efficient electrical motors.

The advantage of the current rotor lies in terms of shape, thickness, and complex geometry, which for an amorphous material cannot be achieved by any manufacturing technique other than AM. The excellent combination of structural and functional properties at the meso- and nanoscale, together with the complex massive geometry, make this amorphous rotor a highly promising SMM component for high-frequency applications, where it could operate with extremely low electric power losses. The scalability of the described AM process for industrial production is deemed very high as a commercial SLM printer, as well as commercially available powder of industrial grade quality, were utilized for the current study.

CRediT authorship contribution statement

Lena Thorsson: Conceptualization, Methodology, Investigation, Writing – review & editing. **Mattias Unosson:** Conceptualization, Methodology. **María Teresa Pérez-Prado:** Investigation, Methodology, Funding acquisition, Supervision, Writing – review & editing. **Xueze Jin:** Investigation, Methodology. **Paola Tiberto:** Investigation, Methodology, Supervision, Writing – review & editing. **Gabriele Barrera:** Investigation, Writing – review & editing. **Bastian Adam:** Investigation, Writing – review & editing. **Nico Neuber:** Investigation, Methodology, Methodology, Writing – review & editing. **Amirhossein Ghavimi:** Investigation, Writing – review & editing. **Maximilian Frey:** Investigation, Methodology. **Ralf Busch:** Conceptualization, Supervision, Writing – review & editing. **Isabella Gallino:** Conceptualization, Methodology, Supervision, Writing – original draft, Data curation, Validation, Writing – review & editing.

Declaration of Competing Interest

The authors declare that they have no known competing financial interests or personal relationships that could have appeared to influence the work reported in this paper.

Acknowledgements

Data availability.

The raw data required to reproduce these findings are available to download from https://doi.org/10.5281/zenodo.5774943. The processed data required to reproduce these findings are available to download from https://doi.org/10.5281/zenodo.5779193.

References

[1] F. Fiorillo, G. Bertotti, C. Appino, M. Pasquale, Soft Magnetic Materials (2016) Wiley Encyclopedia of Electrical and Electronics Engineering. https://doi.org/10.1002/047134608X.W4504.pub2
[2] M.A. Willard, M. Daniil, K.E. Kniping, Nanocrystalline soft magnetic materials at high temperatures: A perspective, Scr. Mater. 67 (6) (2012) 554–559, https://doi.org/10.1016/j.scriptamat.2011.12.043.
[3] J.M. Silveyra, E. Ferrara, D.L. Huber, T.C. Monson, Soft magnetic materials for a sustainable and electrified world, Science 362/6413 (2018) eaao0195, https://doi.org/10.1126/science.aao0195.
[4] A.T. Sankara Subramanian, P. Meenalochini, S. Suba Bala Sathiya, G. Ram Prakash, A review on selection of soft magnetic materials for industrial drives, Mater. Today: Proc. 45 (2021) 1591–1596.
[5] A. Hamler, V. Goričan, B. Šuštaršič, A. Sirc, The use of soft magnetic composite materials in synchronous electric motor, J. Magn. Magn. Mater. 304 (2) (2006) 816–819, https://doi.org/10.1016/j.jmmm.2006.03.003.
[6] E.A. Périgo, J. Jacimovic, F. García Ferré, L.M. Scherf, Additive manufacturing of magnetic materials, Addit. Manuf. 30 (2019) 100870, https://doi.org/10.1016/j.addma.2019.100870.
[7] D. Goll, D. Schuller, G. Martinek, T. Kunert, J. Schurr, C. Sinz, T. Schubert, T. Bernthaler, H. Riegel, G. Schneider, Additive manufacturing of soft magnetic materials and components, Addit. Manuf. 27 (2019) 428–439, https://doi.org/10.1016/j.addma.2019.02.021.
[8] C. Zhang, X. Li, L. Jiang, D. Tang, H. Xu, P. Zhao, J. Fu, Q. Zhou, Y. Chen, 3D Printing of Functional Magnetic Materials: From Design to Applications, Adv. Funct. Mater. 31 (34) (2021) 2102777, https://doi.org/10.1002/adfm.v31.3410.1002/adfm.202102777.
[9] Y.G. Nam, B. Koo, M.S. Chang, S. Yang, J. Yu, Y.H. Park, J.W. Jeong, Selective laser melting vitrification of amorphous soft magnetic alloys with help of double-scanning-induced compositional homogeneity, Mater. Lett. 261 (2020) 127068, https://doi.org/10.1016/j.matlet.2019.127068.
[10] F. Xie, Q. Chen, J. Gao, Y. Li, Laser 3D Printing of Fe-Based Bulk Metallic Glass: Microstructure Evolution and Crack Propagation, J. Mater. Eng. Perform. 28 (2019) 3478–3486, https://doi.org/10.1007/s11665-019-04103-1.
[11] S. Firdosy, N. Ury, J.P. Borgonia, B. McEnerney, R. Conversano, R. Hofer, A. Hermann, H. Ucar, V.A. Ravi, R.P. Dillon, Processing–Microstructure–Property Relationships in a Laser-Deposited Fe-Co-V Alloy, Adv. Eng. Mater. (2021) 2100931, https://doi.org/10.1002/adem.202100931.
[12] T. DebRoy, H.L. Wei, J.S. Zuback, T. Mukherjee, J.W. Elmer, J.O. Milewski, A.M. Beese, A. Wilson-Heid, A. De, W. Zhang, Additive manufacturing of metallic components – Process, structure and properties, Prog. Mater. Sci. 92 (2018) 112–224, https://doi.org/10.1016/j.pmatsci.2017.10.001.
[13] S. Pauly, L. Löber, R. Petters, M. Stoica, S. Scudino, U. Kühn, J. Eckert, Processing metallic glasses by selective laser melting, Mater. Today 16 (1-2) (2013) 37–41, https://doi.org/10.1016/j.mattod.2013.01.018.
[14] H.Y. Jung, S.J. Choi, K.G. Prashanth, M. Stoica, S. Scudino, S. Yi, U. Kühn, D.H. Kim, K.B. Kim, J. Eckert, Fabrication of Fe-based bulk metallic glass by selective laser melting: a parameter study, Mater. Des. 86 (2015) 703–708, https://doi.org/10.1016/j.matdes.2015.07.145.
[15] Z. Mahbooba, L. Thorsson, M. Unosson, P. Skoglund, H. West, T. Horn, C. Rock, E. Vogli, O. Harrisson, Additive manufacturing of an iron-based bulk metallic glass larger than the critical casting thickness, Appl. Mater. Today 11 (2018) 264–269, https://doi.org/10.1016/j.apmt.2018.02.011.
[16] Ł. Zrodowski, B. Wysocki, R. Wróblewski, A. Krawczyńska, B. Adamczyk-Cieślak, J. Zdunek, P. Błyskun, J. Ferenc, M. Leonowicz, W. Święszkowski, New approach of amorphization of alloys with low forming ability via selective laser melting, J. Alloys and Compounds 771 (2019) 769–776, https://doi.org/10.1016/j.jallcom.2018.08.075.
[17] D. Ouyang, W. Xing, N. Li, Y. Li, L. Liu, Structural evolutions in 3D-printed Fe-based metallic glass fabricated by selective laser melting, Addit. Manuf. 23 (2018) 246–252, https://doi.org/10.1016/j.addma.2018.08.020.

[18] C. Zhang, D.i. Ouyang, S. Pauly, L. Liu, 3D printing of bulk metallic glasses, Mater. Sci. Eng. R 145 (2021) 100625, https://doi.org/10.1016/j.mser.2021.100625.

[19] X.D. Nong, X.L. Zhou, Y.X. Ren, Fabrication and characterization of Fe-based metallic glasses by selective laser melting, Opt. Laser Technol. 109 (2019) 20–26, https://doi.org/10.1016/j.optlastec.2018.07.059.

[20] H. Liu, Q.i. Jiang, J. Huo, Y. Zhang, W. Yang, X. Li, Crystallization in additive manufacturing of metallic glasses: A review, Addit. Manuf. 36 (2020) 101568, https://doi.org/10.1016/j.addma.2020.101568.

[21] N. Luo, C. Scheitler, N. Ciftci, F. Galgon, Z. Fu, V. Uhlenwinkel, M. Schmidt, C. Körner, Preparation of Fe-Co-B-Si-Nb bulk metallic glasses by laser powder bed fusion: Microstructure and properties, Mater. Charact. 162 (2020) 110206, https://doi.org/10.1016/j.matchar.2020.110206.

[22] J. Wegner, M. Frey, M. Piechotta, N. Neuber, B. Adam, S. Platt, L. Ruschel, N. Schnell, S.S. Riegler, H.-R. Jiang, G. Witt, R. Busch, S. Kleszczynski, Influence of powder characteristics on the structural and the mechanical properties of additively manufactured Zr-based bulk metallic glass, Mater. Des. 209 (2021) 109976, https://doi.org/10.1016/j.matdes.2021.109976.

[23] M. Frey, J. Wegner, N. Neuber, B. Reiplinger, B. Bochtler, B. Adam, L. Ruschel, S. S. Riegler, H.-R. Jiang, S. Kleszczynski, G. Witt, R. Busch, Thermoplastic forming of additively manufactured Zr-based bulk metallic glass: A processing route for surface finishing of complex structures, Mater. Des. 198 (2021) 109368, https://doi.org/10.1016/j.matdes.2020.109368.

[24] L. Wang, H. Wang, Y. Liu, Z. Fu, T. Peng, J. Shen, S. Zhou, M. Yan, G. Wang, Y. Dai, Selective laser melting helps fabricate record-large bulk metallic glass: Experiments, simulation and demonstrative part, J. Alloys and Compounds 808 (2019) 151731, https://doi.org/10.1016/j.jallcom.2019.151731.

[25] I. Otsuka, K. Wada, Y.u. Maeta, T. Kadomura, M. Yagi, Magnetic properties of Fe-based amorphous powders with high-saturation induction produced by spinning water atomization process (SWAP), IEEE Trans. Magn. 44 (11) (2008) 3891–3894, https://doi.org/10.1109/TMAG.2008.2002249.

[26] X. Qiu, J.W. Thompson, S.J.L. Billinge, PDFgetX2: A GUI-driven program to obtain the pair distribution function from x-ray powder diffraction data, J. Appl. Crystallogr. 37 (4) (2004), https://doi.org/10.1107/S0021889804011744.

[27] A. Ventura Castilho, D. Silva dos Santos, Effect of Sn addition in the microstructure refinement and corrosion resistance of Cu-Zr-Al-Ag Alloy, Mater. Res. 2272 (2019) e20171139, https://doi.org/10.1590/1980-5373-MR-2017-1139.

[28] B. Ingham, M.F. Thoney, X-ray diffraction for characterizing metallic films, Woodhead Publishing Limited (2014), https://doi.org/10.1533/9780857096296.1.3.

[29] C.M. Cepeda-Jiménez, M. Castillo-Rodríguez, M.T. Pérez-Prado, Origin of the low precipitation hardening in magnesium alloys, Acta Mater. 165 (2019) 164–176, https://doi.org/10.1016/j.actamat.2018.11.044.

[30] S. Gates-Rector, T. Blanton, The Powder Diffraction File: A Quality Materials Characterization Database, Powder Diffr. 34 (4) (2019) 352–360, https://doi.org/10.1017/S0885715619000812.

[31] C. Suryanarayana, A. Inoue, Iron-based bulk metallic glasses, Int. Mater. Rev. 58 (3) (2013) 131–166, https://doi.org/10.1179/1743280412Y.0000000007.

[32] A. Plotkowski, J. Pries, F. List, P. Nandwana, B. Stump, K. Carver, R.R. Dehoff, Influence of scan pattern and geometry on the microstructure and soft-magnetic performance of additively manufactured Fe-Si, Addit. Manuf. 29 (2019) 100781, https://doi.org/10.1016/j.addma.2019.100781.

[33] J. Schroers, R. Busch, A. Masuhr, W.L. Johnson, Continuous refinement of the microstructure during crystallization of supercooled melts, Appl. Phys. Lett. 74 (19) (1999) 2806–2808, https://doi.org/10.1063/1.124020.

[34] S. Stanojevic, I. Gallino, H. Aboulfadl, M. Sahin, F. Mücklich, R. Busch, Oxidation of glassy Ni-Nb-Sn alloys and its Influence on the thermodynamics and kinetics of crystallization, Acta Mater. 102 (2016) 176–186, https://doi.org/10.1016/j.actamat.2015.09.009.

[35] M. Eisenbart, U.E. Klotz, R. Busch, I. Gallino, A colourimetric and microstructural study of the tarnishing of gold bulk metallic glasses, Corros. Sci. 85 (2014) 258–269, https://doi.org/10.1016/j.corsci.2014.04.024.

[36] L. Shadowspeaker, M. Shah, R. Busch, On the crystalline equilibrium phases of the $Zr_{57}Cu_{15.4}Ni_{12.6}Al_{10}Nb_5$ bulk metallic glass forming alloy, Scr. Mater. 50 (7) (2004) 1035–1038.

[37] I. Gallino, R. Busch, Relaxation pathways in metallic glasses, JOM- J. Min. Met. Mat. S. 69 (11) (2017) 2171–2177, https://doi.org/10.1007/s11837-017-2573-6.

[38] I. Gallino, M.B. Shah, R. Busch, Enthalpy relaxation and its relation to the thermodynamics and crystallization of the $Zr_{58.5}Cu_{15.6}Ni_{12.8}Al_{10.3}Nb_{2.8}$ bulk metallic glass-forming alloy, Acta Mater. 55 (4) (2007) 1367–1376.

[39] M. Frey, R. Busch, W. Possart, I. Gallino, On the thermodynamics, kinetics, and sub-T_g relaxations of Mg-based bulk metallic glasses, Acta Mater. 155 (2018) 117–127.

[40] B. Bochtler, O. Gross, I. Gallino, R. Busch, Thermo-physical characterization of the $Fe_{67}Mo_6Ni_{3.5}Cr_{3.5}P_{12}C_{5.5}B_{2.5}$ Bulk Metallic Glass Forming Alloy, Acta Mater. 118 (2016) 129–139, https://doi.org/10.1016/j.actamat.2016.07.031.

[41] F.E. Luborsky, Amorphous Metallic Alloys, Elsevier, 1983.

[42] G. Herzer, Nanocrystalline soft magnetic alloys, Handbook of Magnetic Mater. 10 (1997) 415–462, https://doi.org/10.1016/S1567-2719(97)10007-5.

[43] W. Yang, H. Liu, L. Xue, J. Li, C. Dun, J. Zhang, Y. Zhao, B. Shen, Magnetic properties of $(Fe_{1-x}Ni_x)_{72}B_{20}Si_4Nb_4$ (x=0.0–0.5) bulk metallic glasses, J. Magnetism Magnetic Mater. 335 (2013) 172–176, https://doi.org/10.1016/j.jmmm.2013.02.004.

[44] B.D. Cullity, C.D. Graham, Introduction to Magnetic Materials, Wiley-IEEE Press, 2008, 2nd Edition. ISBN:978-0-471-47741-9. https://doi.org/10.1002/9780470386323

[45] T.N. Lamichhane, L. Sethuraman, A. Dalagan, H. Wang, J. Keller, M.P. Paranthamana, Additive manufacturing of soft magnets for electrical machines—a review, Mater. Today Phys. 15 (2020) 100255–100277, https://doi.org/10.1016/j.mtphys.2020.100255.